RESEARCH ARTICLE

CrossMark

Investigation of shock–acoustic-wave interaction in transonic flow

Antje Feldhusen-Hoffmann[1] · Vladimir Statnikov[1] · Michael Klaas[1] · Wolfgang Schröder[1]

Abstract
The buffet flow field around supercritical airfoils is dominated by self-sustained shock wave oscillations on the suction side of the wing. Theories assume that this unsteadiness is driven by an acoustic feedback loop of disturbances in the flow field downstream of the shock wave whose upstream propagating part is generated by acoustic waves. Therefore, in this study, first variations in the sound pressure level of the airfoil's trailing-edge noise during a buffet cycle, which force the shock wave to move upstream and downstream, are detected, and then, the sensitivity of the shock wave oscillation during buffet to external acoustic forcing is analyzed. Time-resolved standard and tomographic particle-image velocimetry (PIV) measurements are applied to investigate the transonic buffet flow field over a supercritical DRA 2303 airfoil. The freestream Mach number is $M_\infty = 0.73$, the angle of attack is $\alpha = 3.5°$, and the chord-based Reynolds number is $Re_c = 1.9 \times 10^6$. The perturbed Lamb vector field, which describes the major acoustic source term of trailing-edge noise, is determined from the tomographic PIV data. Subsequently, the buffet flow field is disturbed by an artificially generated acoustic field, the acoustic intensity of which is comparable to the Lamb vector that is determined from the PIV data. The results confirm the hypothesis that buffet is driven by an acoustic feedback loop and show the shock wave oscillation to directly respond to external acoustic forcing. That is, the amplitude modulation frequency of the artificial acoustic perturbation determines the shock oscillation.

1 Introduction

Most civil aircraft fly at transonic cruise speed, such that supersonic flow occurs on the suction side of the wings. Under these conditions, the phenomenon of shock wave/turbulent boundary-layer interaction with separation may induce large-amplitude, low-frequency, self-sustaining shock wave oscillations without any external forcing. The initially steady flow becomes unsteady, resulting in variations in lift and drag. This aerodynamic phenomenon is known as transonic buffet. Figure 1 shows the boundary of buffet onset depending on the flight Mach number and the lift coefficient. This study addresses the buffet flow over a supercritical airfoil with a constant cross section in the spanwise direction. That is, the buffet characteristics of a two-dimensional mean flow are discussed. The interaction between the periodic aerodynamic forces and the wing structure may excite periodic inflection and torsion vibrations, i.e., buffeting, of the wing.

The transonic buffet flow field is characterized by large-scale shock wave oscillations whose oscillation frequency f often is given as a reduced frequency $\omega^\star = 2\pi fc/u_\infty$ based on the chord length c and the freestream velocity u_∞. Experimental studies of Stanewsky and Basler (1990) for a CAST7/D0A1 supercritical airfoil revealed that the reduced buffet frequency varies with the freestream Mach number M_∞, the angle of attack α, and the chord-based Reynolds number Re_c. Typical values are in the range of $0.3 \leq \omega^\star \leq 0.6$. The reduced frequency decreases, if a laminar–turbulent transition of the boundary layer is triggered upstream of the shock wave.

Stanewsky and Basler (1990) also showed that the thickness of the boundary-layer downstream of the shock wave varies with the shock wave position, such that its extent is maximum/minimum when the shock is located most upstream/most downstream. Since the strength of the shock wave depends on the pre-shock Mach number, it is a function of the relative velocity of the moving shock wave and the incoming flow. Thus, the shock is strongest when it propagates upstream during a buffet cycle. Furthermore, different kinds of disturbances are found to propagate upstream and downstream in the buffet flow field (Lee 1990). A comprehensive review on self-sustained shock oscillations on

✉ Antje Feldhusen-Hoffmann
a.feldhusen@aia.rwth-aachen.de

[1] Institute of Aerodynamics and Chair of Fluid Mechanics, RWTH Aachen University, Wüllnerstr. 5a, 52062 Aachen, Germany
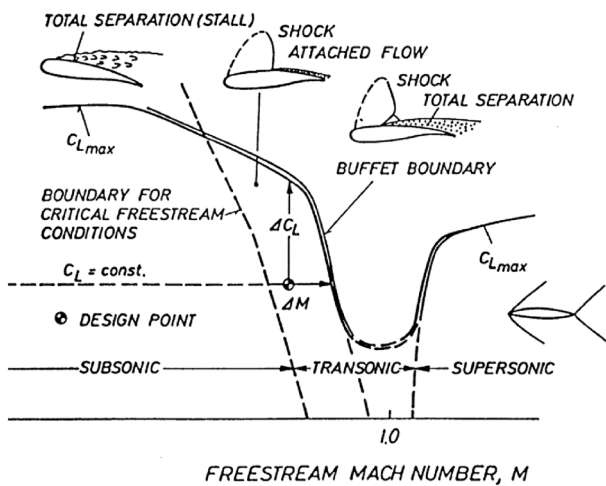
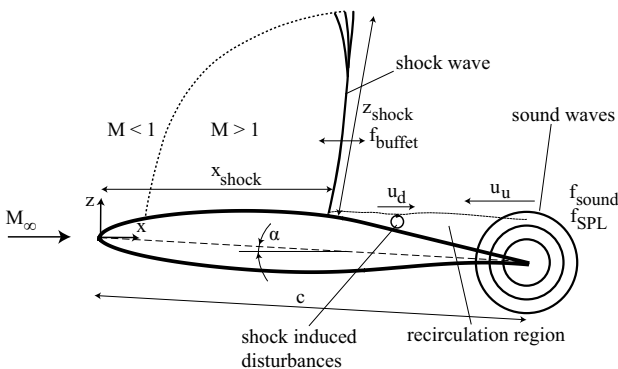**Fig. 1** Buffet boundary (Stanewsky and Basler 1990)

Fig. 2 Main features of the transonic buffet flow over a supercritical airfoil

airfoils at transonic speed has been given by Lee (2001). Another extensive review on recent studies of transonic shock buffet has been given by Giannelis et al. (2017).

In the following, theories on buffet mechanisms will be discussed. Despite intensive research efforts, the mechanisms leading to buffet are still discussed controversially. Widely recognized is a description of the self-sustaining shock oscillation by Lee (1990). In this model, the upstream and downstream propagating disturbances within the flow field downstream of the shock wave form a feedback loop. The model assumes the flow to be fully separated downstream of the shock and the shock to oscillate sinusoidally. The main features of Lee's model are sketched in Fig. 2. According to Lee, the oscillating shock wave generates large-scale turbulent structures that propagate downstream and generate sound waves while passing over the sharp trailing edge of the airfoil. These sound waves propagate upstream outside of the separated recirculation area, as described by Voss (1988) and Finke (1975), and influence

the shock wave movement. Hence, the oscillation frequency is determined by

$$f_{\text{buffet}} = \left(\frac{c - \overline{x}_{\text{shock}}}{u_{\text{d}}} + \frac{c - \overline{x}_{\text{shock}}}{u_{\text{u}}} \right)^{-1}, \qquad (1)$$

i.e., by the time it takes a shock-induced disturbance to convect downstream to the trailing edge plus the time it takes the sound waves originating at the trailing edge to reach the upstream located shock (Lee 2001).

Deck (2005), Xiao et al. (2006), and Hartmann et al. (2012, 2013a, b) found excellent agreement of their numerical and experimental results with Lee's theory. Deck (2005) presented a zonal detached-eddy simulation (DES) method which predicts buffet on the supercritical OTA15A airfoil for a freestream Mach number of $M_{\infty} = 0.73$, a chord-based Reynolds number of $Re_c = 3 \times 10^6$, and an angle of attack of $\alpha = 3.5°$. The author observed instabilities originating at the beginning of the shock-induced boundary-layer separation, growing along the shear layer, and generating upstream propagating acoustic waves. Xiao et al. (2006) simulated the transonic flow over a BGK No.1 supercritical airfoil with unsteady Reynolds-averaged Navier–Stokes equations (URANS) with a two-equation lagged $k - \omega$ turbulence model. For inflow conditions of $M_{\infty} = 0.71$, $Re_c = 20 \times 10^6$, and $\alpha = 1.396°$, the flow field became unsteady evolving shock wave oscillations. They determined the propagation speeds of the traveling pressure waves and thereby the buffet frequency according to Lee's model by space–time correlation of the unsteady pressure field and found good agreement with the actual shock oscillation frequency. Hartmann et al. (2013b) investigated experimentally the buffet flow over a supercritical DRA 2303 airfoil with a chord length of $c = 200$mm at a freestream Mach number of $M_{\infty} = 0.73$, a chord-based Reynolds number of $Re_c = 2 \times 10^6$, and an angle of attack of $\alpha = 3.5°$. The propagation velocities of the disturbances in the flow field were determined by particle-image velocimetry (PIV) and unsteady airfoil surface pressure measurements. Based on the measurement results, Lee's model for the buffet frequency was modified with respect to the distance between the trailing edge and the shock:

$$f_{\text{buffet}} = \left(\frac{c - \overline{x}_{\text{shock}}}{u_{\text{d}}} + \frac{\sqrt{\left(c - \overline{x}_{\text{shock}}\right)^2 + z_{\text{shock}}^2}}{u_{\text{u}}} \right)^{-1}. \qquad (2)$$

The buffet frequency based on Eq. 2 agreed very well with the measured shock oscillation frequency. The experiments by Hartmann et al. (2013b) also revealed that the sound waves generated at the trailing edge possess a high frequency, which is about ten times higher than the shock oscillation frequency. It is expected that the sound pressure

level (SPL) variation frequency of these sound waves corresponds to the buffet frequency, i.e., the shock oscillation frequency. On the one hand, the relative velocity between the incoming flow and the oscillating shock is also stronger when it moves upstream. It triggers stronger disturbances which convect downstream towards the trailing edge. Hence, acoustic waves are generated which force the shock wave to move upstream while interacting with it. The more upstream the shock moves, the wider becomes the recirculation region. This wider distributed vorticity field generates a lower sound pressure field which is why the shock is shifted downstream. This downstream shock motion results in a sharper free-shear layer which enhances the Lamb vector, such that the SPL is increased and the shock moves again upstream. On the other hand, the shock wave is weaker when it moves downstream and excites weaker disturbances which convect downstream towards the trailing edge. As a consequence, acoustic waves with a lower SPL are generated which allow the shock wave to move back to its downstream position while interacting with it. A detailed description of the refined buffet model can be found in Hartmann et al. (2013b).

Furthermore, Hartmann et al. (2013b) also disturbed the flow field by artificial sound waves at a frequency of 1030 Hz which corresponds to the frequency of the sound waves originating naturally at the trailing edge. Note that unlike in the current study, the sound waves in Hartmann et al. (2013b) were not amplitude modulated. The analysis of the shock oscillation frequency spectrum showed that the shock oscillation responds directly to the acoustic perturbation, since the natural buffet frequency of $f_{\text{buffet}} = 129$ Hz as well as the frequency of the external acoustic perturbation are visible as peaks in the frequency spectrum of the shock movement. However, this still does not explain why the shock oscillates naturally with a frequency which is about ten times lower than the frequency of the sound waves originating naturally at the trailing edge during buffet.

Alshabu and Olivier (2008) investigated experimentally the influence of upstream propagating pressure waves appearing naturally in the flow over a supercritical BAC3-11 airfoil on shock waves of different strengths at zero angle of attack for different inflow conditions. Hermes et al. (2012) compared the flow case of Alshabu and Olivier with $M_\infty = 0.71$ and $Re_c = 3.0 \times 10^6$ to their numerical simulations. They highlighted vortices originating and propagating downstream inside the boundary layer and generating sound waves when passing over the trailing edge. These pressure waves, which also propagate upstream, can provoke a shock movement in a flow field which does exhibit buffet. At nearly critical inflow conditions, i.e., $M_\infty = 0.71, Re_c = 2 \times 10^6$ and $M_\infty = 0.72, Re_c = 2 \times 10^6$, these small disturbances may already cause unsteadiness in the flow field. In the region of the maximum airfoil thickness, they coalesce to weak shock

waves which diminish while moving upstream. At supercritical inflow conditions, a shock wave exists on the suction side of the airfoil which interacts with the upstream propagating pressure waves. For a weak shock wave, i.e., $M_\infty = 0.76$ and $Re_c = 1 \times 10^6$, the interaction leads to a degeneration of the shock to a compression wave. Stronger shock waves with $M_\infty = 0.8$ and $Re_c = 3.4 \times 10^6$ are influenced less by the pressure waves. The upstream propagating waves are more massively impaired in their upstream movement by the stronger shock wave, such that they pass around the shock and continue their propagation in the subsonic region.

Although Lee's explanation of the buffet phenomenon is widely accepted, there also exist alternative hypotheses, e.g., in Jacquin et al. (2009), Garnier and Deck (2010), and Crouch et al. (2009). Jacquin et al. (2009) investigated the transonic flow field over a OTA15A supercritical airfoil with intermittent boundary-layer separation at freestream Mach numbers of $0.7 < M_\infty < 0.75$, a chord-based Reynolds number of $Re_c = 3 \times 10^6$, and incidence angles of $2.5° < \alpha < 3.91°$. They applied surface flow visualizations, high-speed schlieren cinematography, steady and unsteady surface pressure measurements, and two-component Laser-Doppler velocimetry (LDV), and found small perturbations that originate at the trailing edge and travel upstream on the suction side and on the pressure side of the airfoil. The authors concluded from their measurements that the upstream traveling perturbations on the pressure side are diffracted by the leading edge of the airfoil, travel downstream on the suction side, and interact with the shock. This led to the assumption that the shock wave is influenced by downstream as well as by upstream traveling acoustic waves. Garnier and Deck (2010) studied the buffet flow case $(M_\infty = 0, 73, \alpha = 3.5°, Re_c = 3 \times 10^6)$ from Jacquin et al. (2009) numerically by applying RANS/LES simulations and zonal detached-eddy simulation. They also assumed that acoustic waves traveling upstream on the pressure side of the airfoil influence via the acoustic feedback loop proposed by Lee (1990) the shock wave. Crouch et al. (2009) performed unsteady Reynolds-averaged Navier–Stokes (URANS) simulations of the transonic flow over an NACA 0012 profile at a freestream Mach number of $M_\infty = 0.76$, a chord-based Reynolds number of $Re_c = 10^7$, and an angle of attack of $\alpha = 3.2°$. They observed pressure waves spreading around the trailing edge and propagating along the airfoil's pressure side until they entered into the sonic zone upstream of the shock wave. From the results of a global instability analysis, Crouch et al. concluded that buffet onset is linked to a global instability of the flow field. Sartor et al. (2015) also found buffet onset to be linked to a global instability mode which they derived from the linearized Navier–Stokes equations. The simulations were performed for an OAT15A supercritical airfoil flow at a freestream Mach number of $M_\infty = 0.73$, a chord-based Reynolds number of $Re_c = 3.2 \times 10^6$, and

incidence angles of $2.5° < \alpha < 7°$. In addition to low-frequency unsteadiness, which is linked to shock wave oscillations, they observed medium-frequency scale unsteadiness which may be present in the separated shear layer and led to broadband Kelvin-Helmholz type instabilities. Even though these studies consider different acoustic-wave propagation paths which do not correspond to the findings of Lee (1990), it has to be noted that all authors emphasize the importance of acoustic waves, which are generated at the trailing edge, for the buffet mechanism.

A deeper understanding of the mechanisms leading to buffet is a must to influence the buffet boundary. The theories on the buffet phenomenon agree on the crucial role of the acoustic waves emanating from the trailing edge. They differ, however, on the mechanisms of their interaction with the recompression shock and, in particular, on the relevant propagation paths. Since the latter aspect is of great interest not only from the theoretical point of view, but also for practical considerations, e.g., positioning of control devices, the sound propagation is first analyzed numerically in this manuscript. As the frequency of the trailing-edge noise is about ten times higher than the buffet frequency, there has to be another low-frequency mechanism present in the flow field which forces the shock wave to oscillate. The shock strength varies with respect to its relative velocity to the incoming flow. The more upstream the shock moves, the wider becomes the recirculation region. This wider distributed vorticity field generates a lower sound pressure field which is why the shock is shifted downstream. This downstream shock motion results in a sharper free-shear layer which enhances the Lamb vector, such that the SPL is increased and the shock moves again upstream. In other words, the sound pressure level of the trailing-edge noise and the frequency of the shock movement are coupled. Therefore, related to Lee's buffet model, the variation in sound generation at the trailing edge is studied next. Then, it is investigated how the feedback loop, which leads to the buffet flow and whose trailing-edge noise represents the upstream propagating part, can be influenced by artificial noise with a varying SPL that is introduced to the flow in the trailing-edge region. To the best of the authors' knowledge, the impact of a varying SPL of external acoustic perturbations to shock oscillations is reported here for the first time in the literature.

Based on the previous discussion, the paper has the following structure. Section 2 describes the experimental setup comprising the wind tunnel, the artificial sound source which will introduce acoustic perturbations to the buffet flow field, the airfoil model, the setup for the particle-image velocimetry measurements, and the flow parameters. In Sect. 3.1, the acoustic wave propagation paths are investigated using large-eddy simulation (LES) results. In Sect. 3.2, the experimental results will be discussed. First, the acoustic environment of

the wind tunnel with the artificial sound source installed is analyzed before investigating the vortex-based sound field for the undisturbed buffet field and studying the impact of the artificial acoustic perturbation on the shock movement. Finally, Sect. 4 summarizes the conclusions and gives an outlook for future research efforts.

2 Experimental setup

2.1 Wind tunnel

All measurements of this study are performed in the trisonic vacuum storage wind tunnel of the Institute of Aerodynamics of the RWTH Aachen University. A sketch of the tunnel is shown in Fig. 3. A compressor evacuates four vacuum tanks with an overall volume of $380\,m^3$ downstream of the closed test section. The air from the tanks is guided through a silica gel based drier and stored in a settling reservoir upstream of the test section under ambient conditions. The drier ensures that the relative humidity of the air is kept below 4% to preclude any influence of the humidity on the shock wave position Binion (1988). To initiate a run, the main quick-acting valve downstream of the diffuser opens and the air flows through the test section. The turbulence intensity of the flow entering the test section is less than 1% (Guntermann 1992). Since the tunnel works intermittently, the measurement time with stable flow conditions is limited to 2–3 s depending on the Mach number. The Mach number can be varied from $M_\infty = 0.3$ to $M_\infty = 4.0$, whereas the Reynolds number depends on the Mach number and on the ambient conditions in the dry-air reservoir. Therefore, the unit Reynolds number $Re\,/\,L$ is restricted to the range of $12 \times 10^6\,m^{-1} \leq Re/L \leq 14 \times 10^6\,m^{-1}$ for the transonic Mach number regime.

The test section possesses a square cross section of $0.4\,m \times 0.4\,m$ and a length of $1.41\,m$. For the investigation of transonic flows, the flexible upper and lower adaptive walls of the test section simulate unconfined flow conditions by solving the 1D-Cauchy integral (Amecke 1985)
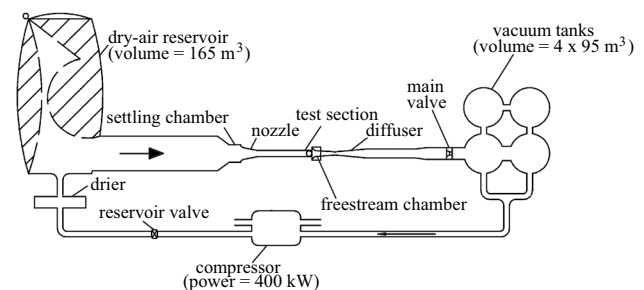

Fig. 3 Sketch of the trisonic wind tunnel of the RWTH Aachen University

based on the steady pressure distribution along each wall measured during the previous run. Besides the steady pressure tubes, whose signals are used for the wall adaption, the top and bottom walls of the test section are equipped with 26 wall mounted pressure transducers Kulite XT-190M-700 mbar D along the centerlines. The signals are recorded by a data acquisition (DAQ) system Gould Nicolet DAStarNet with a sampling rate of 10 kHz, low-pass filtered with a cutoff frequency of 5 kHz, and approximately a hundredfold amplification.

2.2 Artificial sound source

The freestream chamber downstream of the test section offers the possibility to install a loudspeaker, whose end is connected to a horn that points towards the trailing edge of the airfoil model. For the experiments, a BMS-4591 midrange loudspeaker with a power of 150 WAES and a maximum SPL of 136 dB has been employed, since this speaker provides an elevated SPL and fits into the compartment inside the tunnel. The acoustic signal is emitted by an HP32120A signal generator. It consists of a sine wave with a high frequency of f_{sound} whose amplitude is modulated with a low frequency of f_{SPL}, as plotted in Fig. 4. The sampling rate is $f_s = 48,000$Hz and the number of samples is $n = 480,000$. The sound signal is amplified by a 2×2300 W/4 Ohm Camco Vortex-6 amplifier leading to an SPL of 136 dB within quiescent air. This is according to the loudspeaker's data sheet and confirmed by pressure measurements with a Kulite pressure sensor located at $x/c = 0.5267$ on the airfoil's suction side. The amplitudes of the sound signal exiting the loudspeaker are amplified by a horn whose geometry was calculated by the Institute of Technical Acoustics of the RWTH Aachen University (Behler and Bernhard 1998). The distance of the horn exit to the trailing edge of the airfoil model is 480 mm. Figure 5 shows a close-up view of the setup for the generation of the sound waves in the trisonic wind tunnel.
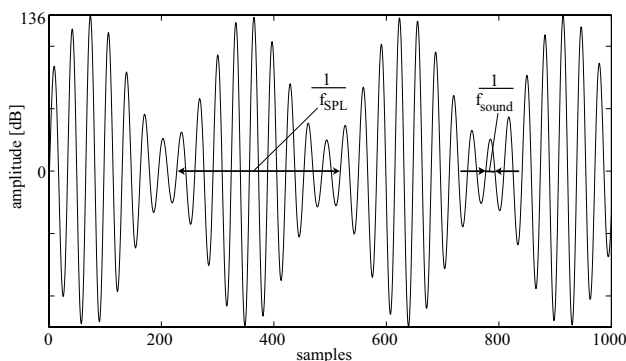

Fig. 4 Sound signal emitted by the artificial sound source
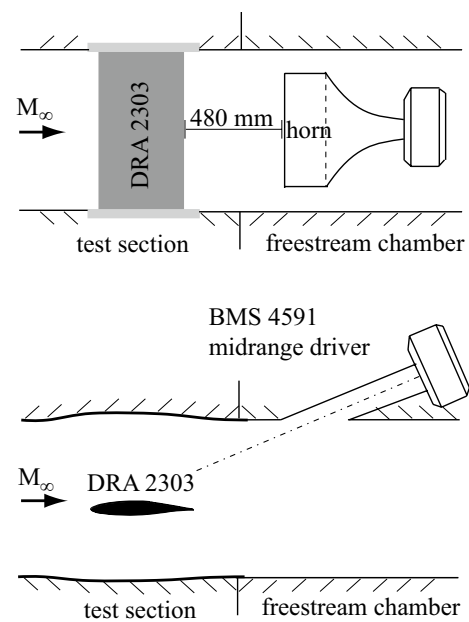

Fig. 5 Top view (top) and side view (bottom) of the adaptive test section and the freestream chamber of the wind tunnel with the sound source and the airfoil model installed

2.3 Airfoil model

The flow over a supercritical laminar-type DRA 2303 profile with a chord length of 0.15 m is measured. It is a two-dimensional model spanning the complete test section width. The relative ratio of the airfoil thickness to chord length is 14% which leads to a blockage of about 5% when mounted inside the adaptive test section. Note that for the wing model with constant cross section in the spanwise direction, the buffet characteristics differ from those found for three-dimensional wings, where the most severe large-scale unsteadiness is found at the wing tip and the flow frequencies are approximately one order of magnitude higher and more broadband (Roos 1985).

The airfoil model is made of two carbon fiber laminate sandwich shells and incorporates a steel beam inside which ensures a rigid mounting in the test section. Laminar-to-turbulent transition is imposed by a 117 μm-thick zigzag stripe located at 5% chord on both suction and pressure side. A photo of the airfoil model is shown in Fig. 6. Note that, although the airfoil model is equipped with probes to measure the steady and unsteady pressure distributions along the centerline in the spanwise direction, these signals will not be discussed in this paper.

2.4 Particle-image velocimetry measurements

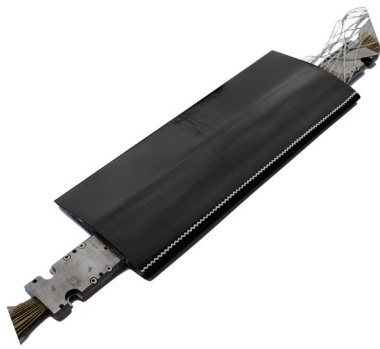In the following, the experimental setups for the high-speed standard (HS-PIV) and the high-speed tomographic

Fig. 6 Supercritical laminar-type DRA 2303 airfoil model

particle-image velocimetry (HS-TPIV) measurements are described. The HS-TPIV measurements will be used to quantify the vortex-based sound field in the trailing-edge region and the impact of the artificial acoustic perturbation on the shock movement is determined by the HS-PIV findings. An overview of the tomographic PIV setup installed at the trisonic wind tunnel facility is given in Fig. 7. The setup for the standard PIV measurements is similar, except that only one high-speed laser and one camera are used. Prior each test run, the dry air inside the tunnel reservoir is seeded with di-ethyl-hexyl-sebacat (DEHS) droplets with a mean diameter of less than 1 μm. For the tomographic
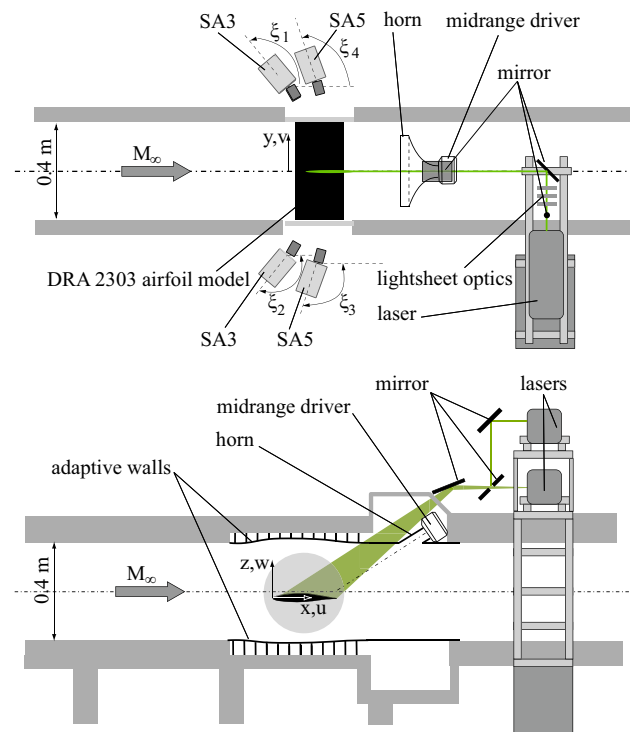
PIV measurements, the seeding concentration was approximately 0.03 ppp (particles per pixel). Inside the test section, the particles are illuminated by one or two high-speed lasers depending on the PIV setup. For the standard PIV, the light of one laser spans a vertical streamwise measurement plane and the measurement region covers the range of $0.41 \leq x/c \leq 0.53$ and $0.06 \leq z/c \leq 0.2$ in the midspan region of the airfoil's suction side. For the tomographic PIV, the two laser beams form a 6 mm thick light volume from $0.8 \leq x/c \leq 1.2$ and $-0.02 \leq z/c \leq 0.36$ near the trailing edge of the airfoil model in the midspan region of the suction side. The locations of the measurement area and the tomographic PIV measurement volume are sketched in Fig. 8.

A system of four Photron high-speed FASTCAMS (two SA3 and two SA5) is used to record the forward scattered light of the seeding particles in the tomographic PIV setup. The corresponding viewing angles of the cameras, which are arranged in Scheimpflug condition, are $\xi_1 = 124°, \xi_2 = 130°, \xi_3 = 111°$, and $\xi_4 = 110°$, as indicated in Fig. 7. For the standard PIV setup, one high-speed camera is installed perpendicular to the measurement plane. For both setups, the images are acquired using the frame straddling technique with a laser pulse separation time of 4 μs. The sampling frequencies are 4000 Hz for the standard PIV and 1000 Hz for the tomographic PIV investigations. Table 1 lists the hardware which was used for the PIV measurements. The evaluation procedures of the raw data are summarized in Table 2. The calibration of the tomographic PIV images was improved by a disparity correction (Wieneke 2008), such that the final maximum calibration error expressed by the maximum RMS of the calibration fit was 0.182 pixel, which is in the expected range of 0.1 pixel to 0.2 pixel (Wieneke 2008). The averaged ghost level of the reconstructed volumes was about 40%.

Concerning the HS-PIV setup, which focuses on the shock wave region, one important parameter for the application of PIV is to provide seeding particles that adequately
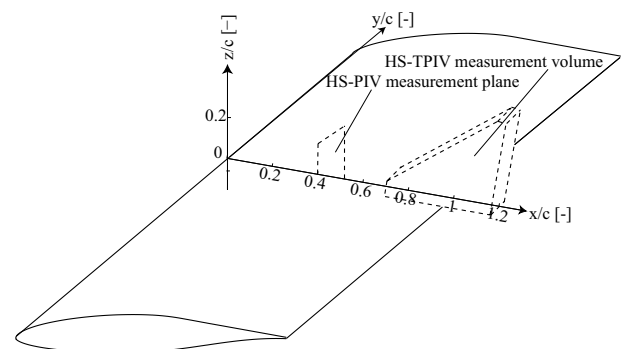

Fig. 7 Schematic of the trisonic wind tunnel and the tomographic PIV setup [(top view (top), side view (bottom)] with the airfoil and the midrange driver installed

Fig. 8 Location of the measurement plane of the standard PIV setup and location of the measurement volume for topmographic PIV

Table 1 Hardware components and settings for standard and tomographic PIV

	Standard PIV	Tomo-PIV
Laser	Darwin Duo 527-100-M Nd:YLF	Darwin Duo 527-100-M Nd:YLF
		Darwin Duo 527-40-M Nd:YLF
Camera	FASTCAM SA3 Model 120K	$2 \times$ FASTCAM SA3 Model 120K
		$2 \times$ FASTCAM SA5 Model 775K-M3
Lens	135 mm Nikon, f\2.8	$4 \times$180 mm Tamron, f\8
Resolution	256 px $\times$ 512 px	1024 px $\times$ 1024 px
$f_{s,PIV}$	4000 Hz	1000 Hz
Measurement time	1.9 s	1.36 s
Captured buffet cycles	~ 320	~ 230

Table 2 Data for standard and tomographic PIV measurements

	Standard-PIV	Tomo-PIV
Software	PIVview, version 3.3.2	DaVis, version 8.2.3
	(ILA_5150 GmbH)	(LaVision)
Evaluation methods	Multi-grid interrogation method	Volumetric self calibration (Wieneke 2008)
		FastMART volume reconstruction
		Multi-pass interrogation method
Outlier detection	Dynamic mean test	Universal outlier detection
	Interpolation	Gaussian smoothing
Final window size	16 px $\times$ 16 px	48 px $\times$ 48 px $\times$ 48 px
Final number of vectors (after masking out)	Approximately 960	Approximately 67510
Window overlap	50%	75%
Final vector spacing	0.62 mm	0.74 mm

follow the flow in the shock wave region. As a measure whether the particles adequately follow the flow, the particle-response time τ_p is used following the approach given by Melling (1986, 1997)

$$\tau_p = \frac{\left(1 + 2.7 Kn_p\right)\rho_p d_p^2}{18\eta}.$$ (3)

Here, Kn_p is the Knudsen number, defined as the relation of the mean free path of the gas molecules and the seeding particle diameter d_p, ρ_p is the density of the seeding, and η is the dynamic viscosity of the fluid. For a total temperature of 293 K, a total pressure of 0.99 bar, and a pre-shock Mach number of 1.2, the resulting particle-response time is 4.04 µs corresponding to a frequency of $f_p = 247$ kHz, such that the particles adequately follow the shock wave movement.

2.5 Flow parameters

For the experiments, the inflow conditions were chosen, such that self-sustained shock wave oscillations occur naturally in the DRA 2303 airfoil flow. These conditions

are known from former experiments, see, e.g., Hartmann et al. (2013b). Based on these previous findings, the airfoil was positioned in the test section at a fixed angle of attack of 3.5°. The Mach number was set to $M_\infty = 0.73$ and the resulting Reynolds number based on the chord length was $Re_c = 1.9 \times 10^6$. In addition to two reference measurements, in the following denoted as cases I and II, where no sound waves were emitted by the loudspeaker, two cases denoted as cases III and IV were investigated. In the latter cases, sound waves were overlaid on the buffet flow field by the artificial sound source. The frequency of the sound waves is $f_{sound} = 1100$ Hz, which corresponds to the frequency of the natural trailing-edge noise, known from Feldhusen et al. (2013). Furthermore, the artificial sound perturbation is amplitude modulated, such that its SPL varies. The amplitude modulation frequency is set to frequencies near the natural buffet frequency of $f_{buffet} = 170$ Hz. One amplitude modulation frequency exceeds the buffet frequency (case III, $f_{SPL} = 175$ Hz) and one amplitude modulation frequency is below the natural buffet frequency (case IV, $f_{SPL} = 165$ Hz) (Table 3).

Table 3 Measurement cases

	Standard-PIV	Tomo-PIV
Reference cases—no acoustic forcing	II	I
$(f_{\text{sound}}, f_{\text{SPL}}) = (1100 \text{ Hz}, 175 \text{ Hz})$	III	
$(f_{\text{sound}}, f_{\text{SPL}}) = (1100 \text{ Hz}, 165 \text{ Hz})$	IV	

3 Results

As mentioned in the Introduction, the theories on the buffet phenomenon agree on the crucial role of the acoustic waves emanating from the trailing edge and differ on the mechanisms of their interaction with the recompression shock and particularly on the relevant propagation paths. To shed light on this controversial aspect, the spatial distribution of the root-mean-square pressure fluctuations, which define the overall SPL, is investigated first in Sect. 3.1. This numerical investigation is essential, since it shows the dominance of the sound propagation path from the trailing edge to the shock via the upper side of the airfoil. This propagation path is the basis of the further experimental analysis discussed in Sect. 3.2.

3.1 Analysis of the acoustic wave propagation

In the following, the propagation of the sound generated at the trailing edge is numerically analyzed. Based on the LES data from Roidl et al. (2011) of the flow around a DRA 2303 profile at $M_{\infty} = 0.72$, $Re_c = 2.7 \times 10^6$, and $\alpha = 3°$, the non-dimensionalized pressure fluctuation field $c_{p'} = p'/\bar{q}$ is shown in Fig. 9a. The highest pressure fluctuations are at the mean recompression shock position where the shock is strongest. It oscillates in the streamwise direction leading to significant variations of the local pressure. The second highest pressure fluctuations occur at the trailing edge that acts as an acoustic source. This is visualized by the propagation of the pressure fluctuations in the radial direction. Figure 9b quantitatively compares the spatial distribution of the pressure fluctuation level $c_{p'}$ along the suction and the pressure side as a function of the relative distance to the trailing edge $(r - r_{\text{TE}})/c = \sqrt{(x - x_{\text{TE}})^2 + (y - y_{\text{TE}})^2}/c$. It is clearly seen that the pressure fluctuations have a local peak at the trailing edge and then continuously decrease along the pressure side when moving upstream to the leading edge. On the suction side, the pressure fluctuations remain at approximately the same high level in the region of the shock-induced separation bubble. Consequently, at the mean shock position, the levels of the pressure fluctuations upstream and downstream of the shock differ by one order of magnitude. The pressure fluctuations from the downstream region clearly dominate. Hence, it can be concluded that the propagation path along the separation region on the suction side has a much stronger
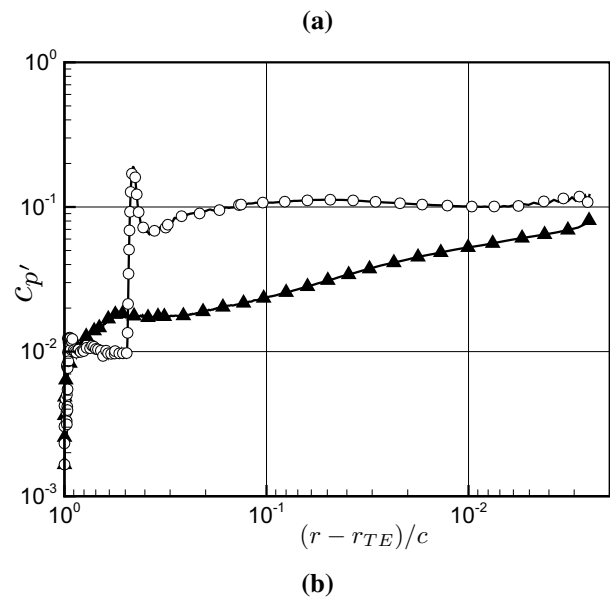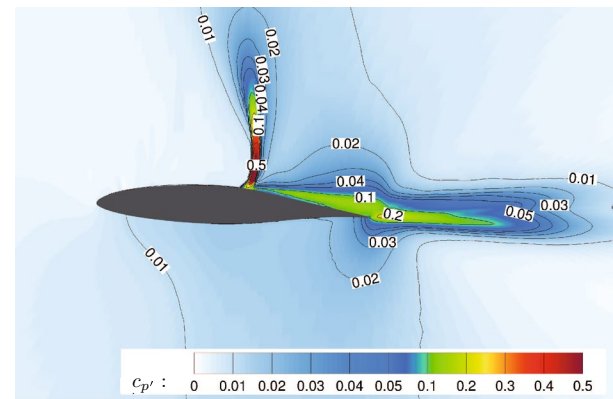

(a)

(b)

Fig. 9 Time-averaged distribution of the non-dimensionalized pressure fluctuations $c_{p'}$ around an DRA 2303 airfoil computed via an LES (Roidl et al. 2011): **a** field view; **b** distribution along the suction (circle) and the pressure side (filled triangle) as a function of the relative distance to the trailing edge

impact on the shock motion than the path along the pressure side and around the leading edge. This fact also justifies the positioning of the acoustic control device, i.e., the loudspeaker, above the separation region downstream of the shock as it is described in Sect. 2.

3.2 Experimental results

This section comprises the description and analysis of the measurement results. For the sake of clarity, it is divided into three parts. In Sect. 3.2.1, the acoustic environment of the wind tunnel, and, hence, in the test section, is analyzed using the signals of unsteady pressure sensors installed inside the lower test section wall. Section 3.2.2 contains the analysis of the distribution of the three-dimensional Lamb vector,

which is defined by the outer product of the vorticity and the velocity vector, obtained by tomographic PIV measurements to determine the vortex-based sound field in the trailing-edge region during buffet flow. Finally, in Sect. 3.2.3, the impact of external acoustic perturbations on the shock movement during buffet is discussed based on the standard PIV measurements conducted in the shock wave region.

3.2.1 Acoustic environment of the wind tunnel configuration

As a first step, the acoustic environment of the wind tunnel is analyzed to detect disturbances due to tunnel noise and to ensure that the sound signal emitted by the loudspeaker covers the whole test section. When the artificial sound source is installed inside the tunnel downstream of the test section, the horn presents a cavity to the flow field, which might cause additional sound.

The acoustic environment of the wind tunnel is analyzed using the pressure signal of two transducers installed along the centerline of the bottom test section wall, namely, the transducer installed beneath the trailing edge at $x/c = 1$ and the transducer installed upstream of the wing model at $x/c = -3.58$. During these measurements at $M_\infty = 0.73$, the airfoil model is not installed inside the test section, i.e., the wind tunnel is operated with an empty test section.

Figure 10 shows the power-spectral density (PSD) distributions of the sensors for the reference case II, where no sound is emitted by the loudspeaker, and exemplary for case III, where sound waves with $f_{sound} = 1100$ Hz and $f_{SPL} = 175$ Hz are emitted by the loudspeaker. The power-spectral analysis of the unsteady pressure signals is done using Matlab's *pwelch* function with a window size of 2048 samples and an overlap of 1024 samples. The distributions in Fig. 10 reveal that the installation of the artificial sound source introduces disturbances at a frequency
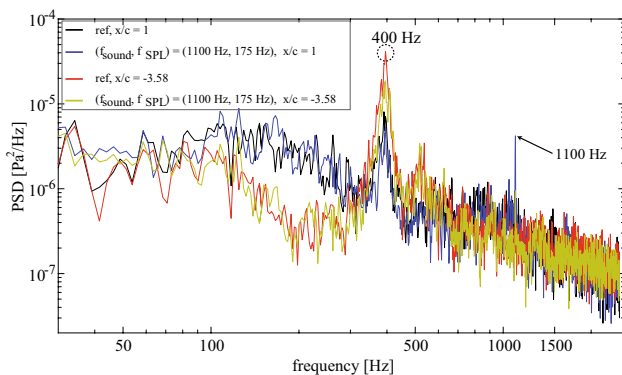

Fig. 10 Power-spectral density of the lower test section wall transducer signals installed beneath the trailing edge at $x/c = 1$ and far upstream of the wing model at $x/c = -3.58$ for the reference case II (no acoustic forcing) and case III ($f_{sound} = 1100$ Hz, $f_{SPL} = 175$ Hz)

of approximately 400 Hz to the flow field, since they did not occur in the measurements without the artificial sound source in Feldhusen et al. (2015). The frequency of 400 Hz corresponds to the frequency of the first Rossiter mode (Rossiter 1964), considering that the horn represents a geometry which is similar to an open cavity in the flow field. As expected, additional pressure waves appear in the flow field when the loudspeaker is on. In other words, cases III and IV—the latter is not shown in Fig. 10—show a distinct peak in the power spectrum at $f = 1100$ Hz. Note that only the high frequency of the artificial sound $f_{sound} = 1100$ Hz is evident in the power spectrum, whereas the amplitude modulation frequency $f_{SPL} = 175$ Hz cannot be detected in the PSD plots.

In summary, the results show the perturbations defining the flow in the empty test section. The frequency of approximately 400 Hz is due to the cavity and the high-frequency sound of 1100 Hz is artificially generated by the loudspeaker. However, the amplitude modulation frequency of 175 Hz, the variation of which defines different SPLs, is not observed in the power-spectral density distributions. This fact is of interest in the following discussion of the interaction of the acoustic waves and the shock movement.

3.2.2 Analysis of vortex-sound source distributions

The three-dimensional velocity field is captured by time-resolved tomographic particle-image velocimetry (PIV) in the trailing-edge region of the airfoil model for the reference case I, where the loudspeaker is turned off, to gain information about the generation of vortex sound. The acoustic perturbation equations (APE) are considered to propagate the trailing-edge noise (Ewert and Schröder 2003). The APE-4 system (Ewert and Schröder 2003) reads

$$\frac{\partial p'}{\partial t} + \overline{a^2}\nabla \cdot \left(\overline{\rho}\boldsymbol{u}' + \overline{\boldsymbol{u}}\frac{p'}{\overline{a^2}}\right) = \overline{a^2}(q_c + q_e),\tag{4}$$

$$\frac{\partial \boldsymbol{u}'}{\partial t} + \nabla\left(\overline{\boldsymbol{u}}\cdot\boldsymbol{u}'\right) + \nabla\left(\frac{p'}{\overline{\rho}}\right) = \boldsymbol{q}_m,\tag{5}$$

where the bar denotes the time-averaging operator and the prime terms are the fluctuating quantities. The right-hand side source terms are

$$q_c = -\nabla \cdot \left(\rho'\boldsymbol{u}'\right)',\tag{6}$$

$$q_e = -\frac{\partial \rho_e}{\partial t} - \nabla \cdot \left(\rho_e\overline{\boldsymbol{u}}\right), \quad \text{and}\tag{7}$$

$$\boldsymbol{q}_m = -(\omega \times \boldsymbol{u})' - \left(\nabla\frac{|\boldsymbol{u}'|^2}{2}\right)' + \nabla\frac{p'}{\overline{\rho}} - \left(\frac{\nabla p}{\rho}\right)'.\tag{8}$$

For trailing-edge noise, which is dominant in the current analysis, the Lamb vector, i.e., the vorticity–velocity cross product

$$\mathbf{L}' = \boldsymbol{\omega} \times \mathbf{u} - \overline{\boldsymbol{\omega} \times \mathbf{u}}, \tag{9}$$

is the major source term. The method to determine the sound field is similar to that of Schröder et al. (2005), who computed the Lamb vector divergence from PIV data to calculate the trailing-edge noise.

In general, the DRA 2303 buffet flow field is characterized by a shock wave on the suction side, which has its mean streamwise position at $x/c = 0.49$ and oscillates with a buffet frequency of $f_{\mathrm{buffet}} = 170$ Hz. The strong shock wave/turbulent boundary-layer interaction induces a full separation of the boundary-layer downstream of the interaction. The previous measurements by Feldhusen et al. (2013) showed that the recirculation region downstream of the shock has its maximum/minimum wall-normal extent if the shock is in its most upstream/most downstream position. Hence, since the shock wave itself is not included in the HS-TPIV measurement volume, the extent of this recirculation region is used as a criterion to detect the shock wave position. Therefore, the inclination of a streamline just above the recirculation region to the x-axis is tracked. When the shock wave is located most upstream/most downstream, the inclination of this streamline is maximum/minimum.

Figure 11 illustrates, based on the contours of the phase-averaged streamwise velocity component $\overline{u}$, which was additionally averaged in the spanwise direction, i.e., over 12 vectors, the extent of the recirculation region based on the velocity fields measured by HS-TPIV for the shock in its most upstream position (Fig. 11a) and its most downstream position (Fig. 11b). The solid lines indicate the shock wave position and the upper edge of the separation region. It is evident from the plots that the extent of the separation region is a reliable indicator for the shock position, since, e.g., the difference in its vertical extent is on the order of $z/c = 0.08$ for the both extrema. These data are used to calculate the phase-averaged perturbed Lamb vector distribution: $\mathbf{L}'_{\mathrm{up/down}} = (\boldsymbol{\omega} \times \mathbf{u})_{\mathrm{up/down}} - \overline{\boldsymbol{\omega} \times \mathbf{u}}$.

Figure 12 shows the phase-averaged contour plots of the absolute value of the perturbed Lamb vector. The change in sign in the Lamb vector distribution results from the relative signs of the velocity and vorticity in the phase-averaged fields. In the outer shear layer region, higher values of the perturbed Lamb vector can be found for the most upstream located shock wave (Fig. 12a). However, in the region near the trailing edge, the values of the perturbed Lamb vector exceed the temporal mean values for the most downstream located shock wave (Fig. 12b). These results confirm the assumption of Lee (1990) and Hartmann et al. (2013b) that more sound is generated at the trailing edge when the shock is located most downstream. The sound waves of this
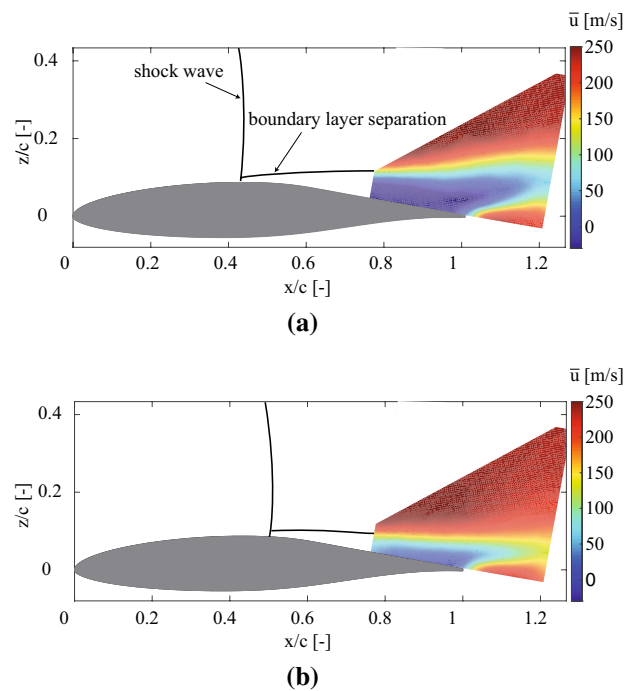
(a)

(b)

Fig. 11 Contours of the phase-averaged and spanwise-averaged streamwise velocity component u; the shock wave and the separation of the boundary layer are indicated using solid black lines. **a** Most upstream located shock. **b** Most downstream located shock

increased SPL will force the shock wave to move upstream when propagating upstream and interacting with the shock wave.

3.2.3 Impact of the artificial sound waves

For the analysis of the influence of sound waves at varying SPL on the shock oscillation of a buffet flow field, the artificial sound waves are emitted by the loudspeaker installed downstream of the airfoil's trailing edge in the upper wind tunnel wall. The data for this analysis were obtained using standard PIV measurements focusing on the shock region. Besides the reference case, where no sound waves are emitted by the loudspeaker, two cases with overlaid sound $(f_{\mathrm{sound}}, f_{\mathrm{SPL}}) = (1100$ Hz, 175 Hz$)$ and $(f_{\mathrm{sound}}, f_{\mathrm{SPL}}) = (1100$ Hz, 165 Hz$)$ denoted as cases III and IV are investigated. The shock wave position is tracked to determine its oscillation frequency. As indicated in Fig. 13, the mean streamwise shock position is defined as the position on a streamline at approximately $z/c = 0.121$, i.e., at half of the height of the measurement area, where the Mach number is equal to one. The local speed of sound to compute the Mach number is determined by the PIV velocity data and the local static temperature obtained by applying the energy equation using the total temperature, measured in the air storage of the wind tunnel prior to each run.
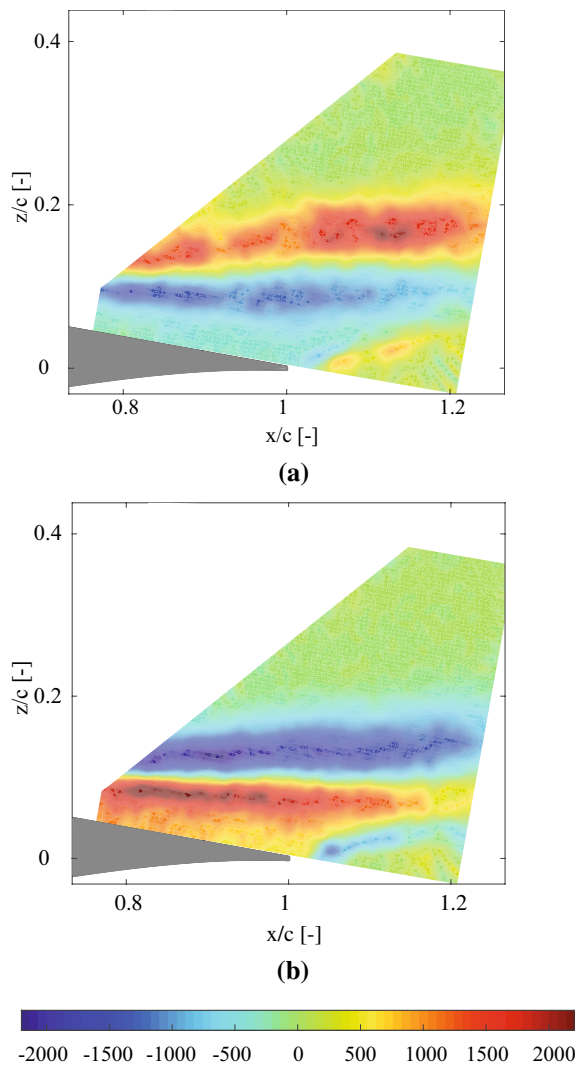
(a)

(b)

$\overline{L'}$

-2000   -1500   -1000   -500   0   500   1000   1500   2000

Fig. 12 Contours of the phase-averaged and spanwise-averaged absolute value of the perturbed Lamb vector $\overline{L'}$. **a** Most upstream located shock. **b** Most downstream located shock
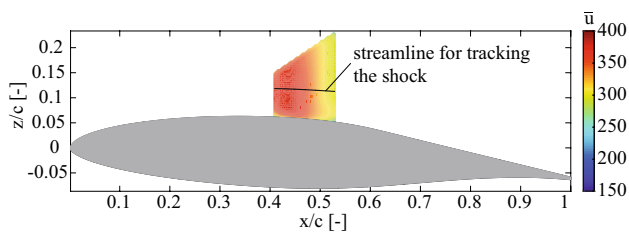

Fig. 13 Contours of the streamwise velocity component, averaged over all time steps
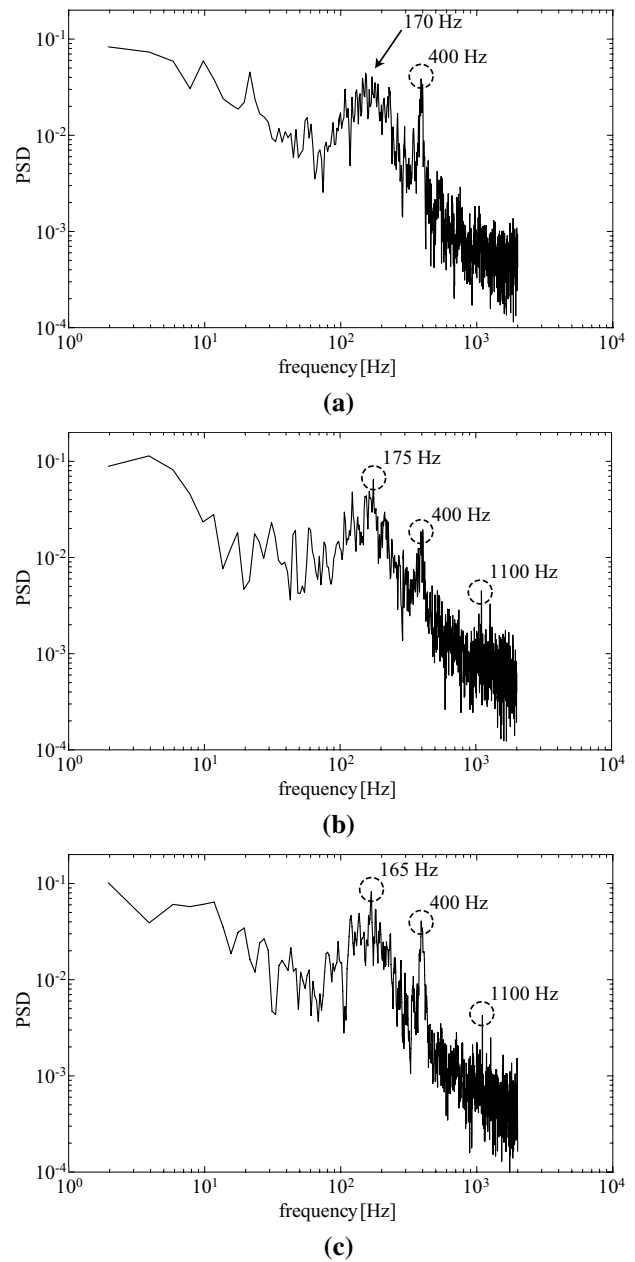

(a)

(b)

(c)

Fig. 14 Power-spectral analysis of the shock wave movement for reference case II without artificial sound field and cases III and IV with artificial sound. **a** Reference case II: no artificial sound field. **b** Case III: $(f_{sound}, f_{SPL}) = (1100 \text{ Hz}, 175 \text{ Hz})$. **c** Case IV: $(f_{sound}, f_{SPL}) = (1100 \text{ Hz}, 165 \text{ Hz})$

In Fig. 14, the power-spectral distributions of the shock wave movement for the three measurement cases are compared. For reference case II, the spectrum peaks at the natural buffet frequency of $f_{buffet} = 170$ Hz, which is known from

the previous studies (e.g. Feldhusen et al. 2015). Moreover, the distributions in Fig. 14b, c show an increased level at the natural buffet frequency. As discussed above, all three spectra show a distinct peak at a frequency of 400 Hz, which corresponds to the frequency of the first Rossiter mode of the cavity. For cases III and IV, i.e., for flow fields with artificially introduced sound, Fig. 14b, c, additional peaks occur at the frequency of the artificial sound signal

$f_\text{sound} = 1100$ Hz and at the frequencies of its amplitude modulation $f_\text{SPL} = 175$ Hz and $f_\text{SPL} = 165$ Hz, respectively. These results show that the shock directly responds to the SPL in the flow field. That is, the disturbances due to the cavity in the tunnel setup, the frequency of the overlaid sound field, and the frequency of the SPL variation, i.e., the amplitude modulation frequency of the artificially generated sound field, are evident in the spectral distributions. Considering the spectral distributions in the frequency range near the natural buffet frequency, i.e., in the vicinity of $f_\text{buffet} = 170$ Hz, it can be stated that the shock oscillation reacts to the artificial amplitude modulation frequency. In other words, the shock motion is determined by the external acoustic perturbation. This evidences the dominant role of the acoustic field for the buffet phenomenon.

4 Conclusion

The transonic flow field over a supercritical DRA 2303 airfoil model was experimentally investigated by time-resolved standard and tomographic particle-image velocimetry measurements. The freestream parameters were $M_\infty = 0.73$, $\alpha = 3.5°$, and the chord-based Reynolds number was $Re_c = 1.9 \times 10^6$. Under these conditions, a self-sustaining shock wave oscillation, i.e., buffet, develops on the suction side of the airfoil.

In an LES-based analysis, it has been shown that the pressure fluctuations propagating over the suction side dominate the interaction with the shock to justify the location of the artificial acoustic perturbation source, i.e., the loudspeaker.

In the first part of the experimental analysis, the perturbed Lamb vector, which is the major source term in a shear-driven acoustic field, has been determined from the time-resolved three-dimensional velocity field obtained by the high-speed tomographic PIV measurements in the trailing-edge region. The findings show that the SPL is highest near the trailing edge when the shock wave is located farthest downstream during the buffet cycle. This result confirms the buffet model introduced by Lee (1990), which was refined by Hartmann et al. (2013b) and which states that the feedback loop of a buffet flow is driven by acoustic waves with varying SPL originating at the trailing edge, propagating upstream, and interacting with the shock wave.

In the second experimental part, the buffet flow field has been artificially perturbed by an acoustic field emitted by a loudspeaker installed downstream of the test section in the upper wind tunnel wall. The sound waves possessed the high frequency $f_\text{sound} = 1100$ Hz and their SPL varied with frequencies of $f_\text{SPL} = 175$ Hz and $f_\text{SPL} = 165$ Hz near the natural buffet frequency of $f_\text{buffet} = 170$ Hz. Additional sound waves with a frequency of 400 Hz were present in the test section, since the horn, which is connected to the loudspeaker, presents an open cavity disturbance to the outer flow. Applying standard PIV in the shock wave region, the frequency spectra of the shock wave oscillation were obtained for a reference case, i.e., without artificial sound and two cases with an induced acoustic field. For all cases, the spectra show an increased level around the natural buffet frequency of 170 Hz. Furthermore, a distinct peak is visible in the spectra at 400 Hz. This frequency is related to the first mode of the cavity flow. The shock wave oscillation reacts directly to the external acoustic forcing of the loudspeaker. That is, the frequency of the artificial sound signal $f_\text{sound} = 1100$ Hz and the frequencies of the amplitude modulation $f_\text{SPL} = 165$ Hz and $f_\text{SPL} = 175$ Hz are evident. These findings further show the strong impact of acoustic waves on the shock oscillation, i.e., the buffet phenomenon, and thus confirm the model of Lee (1990) and Hartmann et al. (2013b). They are the basis for future work regarding actively influencing or suppressing shock wave oscillations as well as investigations concerning the mechanism of buffet onset.

References

Alshabu A, Olivier H (2008) Unsteady wave phenomena on a supercritical airfoil. AIAA J 46:2066–2073

Amecke J (1985) Direkte Berechnung von Wandinterferenzen und Wandadaption bei zweidimensionaler Strömung in Windkanälen mit geschlossenen Wänden. Technical report, DFVLR-FB, pp 85–62

Behler GK, Bernhard A (1998) Measuring method to derive the lumped elements of the loudspeaker thermal equivalent circuit. In: Audio engineering society convention 104

Binion TW (1988) Potentials for Pseudo-Reynolds Number Effects. In: Reynolds number effects in transonic flow. Technical report, AGARD 303, sec. 4

Crouch J, Garbaruk A, Magidov D, Travin A (2009) Origin of transonic buffet on aerofoils. J Fluid Mech 628:357–369

Deck S (2005) Numerical simulation of transonic buffet over a supercritical airfoil. AIAA J 43(7):1556–1566

Ewert R, Schröder W (2003) Acoustic perturbation equations based on flow decomposition via source filtering. J Comput Phys 188:365–398

Feldhusen A, Hartmann A, Klaas M, Schröder W (2013) Impact of alternating trailing-edge noise on buffet flows. AIAA 2013:3028

Feldhusen A, Klaas M, Schröder W (2015) High-speed tomographic PIV measurements of buffet flow over a supercritical airfoil with artificially introduced sound waves. In: 11th international symposium on particle image velocimetry—PIV15 Santa Barbara, California

Finke K (1975) Unsteady shock–wave boundary-layer interaction on profiles in transonic flows. Technical report, AGARD-CPP-168, Paper No. 28

Garnier E, Deck S (2010) Large-Eddy simulation of transonic buffet over a supercritical airfoil. In: Direct and large-eddy simulation VII, ERCOFTAC Series, vol 13. Springer, Berlin.

Giannelis N, Vio G, Levinski O (2017) A review of recent developments in the understanding of transonic shock buffet. Prog Aerosp Sci. https://doi.org/10.1016/j.paerosci.2017.05.004

Guntermann P (1992) Entwicklung eines Profilmodells mit variabler Geometrie zur Untersuchung des Transitionsverhaltens in kompressibler Unterschallströmung. Ph.D. thesis, RWTH Aachen University

Hartmann A, Klaas M, Schröder W (2012) Time-resolved stereo piv measurements of shock-boundary layer interaction on a supercritical airfoil. Exp Fluids 52:591–604

Hartmann A, Klaas M, Schröder W (2013a) Coupled airfoil heave/pitch oscillations at buffet flow. AIAA J 51(7):1542–1552

Hartmann A, Feldhusen A, Schröder W (2013b) On the interaction of shock waves and sound waves in transonic buffet flow. Phys Fluids 25:026101

Hermes V, Klioutchnikov I, Olivier H (2012) Numerical investigation of unsteady wave phenomena for transonic airfoil flow. Aerosp Sci Technol 25:224–233

Jacquin L, Molton P, Deck S, Maury B, Soulevant D (2009) Experimental study of shock oscillation over a transonic supercritical profile. AIAA J 47(9):1985–1994

Lee BKH (1990) Oscillatory shock motion caused by transonic shock boundary layer interaction. AIAA J 28(5):942–944

Lee BKH (2001) Self-sustained shock oscillations on airfoils at transonic speeds. Prog Aerosp Sci 37:147–196

Melling A (1986) Seeding gas flows for laser anemometry. Technical report, AGARD CP-399: Conference on advanced instrumentation for aero engine components, pp 8.1–8.11

Melling A (1997) Tracer particles and seeding for paticle image velocimetry. Meas Sci Technol 8:1406–1416

Roidl B, Meinke M, Schröder W (2011) Zonal RANS-LES computation of transonic airfoil flow. AIAA 2011:3974

Roos F (1985) The buffet pressure field of a high-aspect-ratio swept wing. AIAA 1985:1609

Rossiter JE (1964) Wind-tunnel experiments on the flow over rectangular cavities at subsonic and transonic speeds. Technical report, Aero REs Counc R&M, No. 3438

Sartor F, Mettot C, Sipp D (2015) Stability, receptivity, and sensitivity analyses of buffeting transonic flow over a profile. AIAA J 53(7):1374–1980

Schröder A, Herr M, Lauke T, Dierksheide U (2005) Measurements of trailing-edge-noise sources by means of time-resolved PIV. In: 6th International symposium on particle image velocimetry, vol 2, pp 1–8

Stanewsky E, Basler D (1990) Experimental investigation of buffet onset and penetration on a supercritical airfoil at transonic speeds. Technical report, AGARD CP-483, Paper 4

Voss R (1988) Über die Ausbreitung akustischer Störungen in transsonischen Strömungsfeldern von Tragflügeln. Technical report, DFVLR 88-13, Institut für Aeroelastik, Georg-August-Universität Göttingen

Wieneke B (2008) Volume self-calibration for 3D particle image velocimetry. Exp Fluids 45:549–556

Xiao Q, Tsai M, Liu F (2006) Numerical study of transonic buffet on a supercritical airfoil. AIAA J 44(3):621–628